Hybrid TPMS-Based Architectured Materials (HTAM) for Enhanced Specific Stiffness Using Data-Driven Design

Jinwook Yeo,[1] Samantha Cheung,[2] X. Wendy Gu,[2] and Seunghwa Ryu[*1]

Affiliations

[1] Department of Mechanical Engineering, Korea Advanced Institute of Science and Technology (KAIST), 291 Daehak-ro, Yuseong-gu, Daejeon 34141, Republic of Korea.

[2] Department of Mechanical Engineering, Stanford University, Stanford, CA 94305, USA

[*] Corresponding author Email: S. Ryu (ryush@kaist.ac.kr)

Keywords

Hybrid TPMS-Based Architectured Materials (HTAM), Architectured Materials, Data-driven Optimization, Multi-objective Bayesian Optimization (MBO), Additive Manufacturing

Abstract

This study introduces hybrid TPMS-based architectured materials (HTAM), achieved by superimposing several triply periodic bicontinuous structures (TPBSs). This approach allows for the creation of structures that were previously unattainable using conventional designs. We investigate the optimization of these architectured materials to enhance mechanical stiffness while reducing weight. To explore this expanded design space and identify optimal designs, we employed multi-objective Bayesian optimization (MBO) integrated with Gaussian process regression (GPR). By utilizing both the probability of hypervolume improvement (PHVI) and expected hypervolume improvement (EHVI) acquisition functions in parallel during the optimization process, we improved the efficiency of time and data usage. This facilitated the development of HTAM that form a Pareto front, pushing the upper bound in the relative density and relative stiffness space. The optimized HTAM exhibited markedly higher specific Young's modulus across various relative densities compared to conventional structures. Following optimization and manufacturability considerations, selected HTAM designs were fabricated using selective laser sintering (SLS) at the macro scale and two-photon polymerization (2PP) at the micro scale. Compression tests confirmed the superior stiffness and exceptional yield strength of the HTAM structure, validating their potential for advanced engineering applications.

1. Introduction

The quest for materials with exceptional mechanical properties has been a central focus in materials science and engineering. Traditional materials, constrained by their atomic composition and structure, often fail to meet the growing demands of modern industries. Structural engineering offers a promising solution by manipulating material architecture at the continuum scale to achieve superior properties. Notable examples include structural composites [1-4], and porous materials [5-7] , which exhibit novel behaviors through controlled structural arrangements.

However, the complexity of these advanced structures often poses significant challenges for traditional manufacturing methods like machining, casting, and molding. Although various advanced techniques have been proposed for creating porous structures [8-10], precise control over pore characteristics (shape, size, and connectivity) remains difficult. This limitation restricts design flexibility and hinders the practical application of these materials [11-13]. Additive manufacturing has emerged as a transformative solution, offering the precision and scalability necessary to fabricate intricate structures and utilize the full potential of advanced structures.

Architectured materials with precisely controlled structural features have gained significant attention for their exceptional mechanical properties [14-16]. Their superior mechanical characteristics make them particularly valuable in industries such as aerospace, defense, automotive, and biomedical engineering [17-23]. Among these materials, shell-based triply periodic bicontinuous structures (TPBS) are notable for their high specific stiffness and strength, derived from minimized stress concentrations due to their smooth geometries [24-27], which contrasts with other types such as strut-based and plate-based structures [28-33]. Although previous research has focused on optimizing basic TPBS parameters like density and thickness, these efforts have typically been confined to a narrow design space, highlighting the need for more sophisticated approaches [24-27].

To overcome this limitation, we propose hybrid TPMS-based architectured materials (HTAM), structures that are achieved by the superposition of two or more TPBS equations. This approach significantly expands the design space. To efficiently explore this space and identify optimal HTAM designs with high stiffness and low density, we employ multi-objective Bayesian optimization (MBO) with Gaussian process regression (GPR). Unlike previous methods that rely solely on either the probability of hypervolume improvement (PHVI) or expected hypervolume improvement (EHVI), our optimization process leverages both simultaneously. This approach allows for a balanced combination of exploration (reducing uncertainty of the surrogate model) and exploitation (identifying optimal design), thereby enhancing data efficiency. Additionally, using both acquisition functions in parallel improves

computational efficiency by enabling the simultaneous sampling of multiple data points in each iteration.

Using the optimization results, we selected candidate HTAM designs for fabrication, taking manufacturability into account. The structures were then fabricated at different scales (macro/micro) using selective laser sintering (SLS) and two-photon polymerization (2PP) additive manufacturing. Compression testing confirmed the superior stiffness of HTAM, both in the elastic region and beyond.

2. Method

In this study, we developed HTAM by leveraging data-driven design. HTAM are derived from TPBS, which are mathematically defined volumetric structure using level-set equations extended from TPMS – a surface geometry, as shown in Figure 1(a). Building on this concept, HTAM were generated through the linear combination of two or more TPMS level-set equations, thereby expanding design space to achieve previously unattainable 3D architectures as depicted in Figure 1(b). To efficiently navigate this expanded design space and identify optimized structures with high elastic modulus, generative design strategies known as MBO with GPR were used. Unlike previous studies that typically rely on a single acquisition function, we simultaneously utilized multiple acquisition functions, including PHVI and EHVI to improve optimization efficiency and design space exploration. Following computational optimization, we fabricated the selected HTAM and control structures using two advanced additive manufacturing techniques: SLS for macro-scale production and 2PP for micro-scale fabrication. Finally, compression tests were conducted to evaluate the stiffness of the structures and validate the effectiveness of our optimization approach and designs. By integrating data-driven design algorithm, high-precision manufacturing, and experimental validation, this method provides a comprehensive pathway for developing high-performance architectured materials across multiple scales.

2.1 Data Generation and Automation

To define a single HTAM, the proportion (r_1, r_2, …, r_{10}) of each TPMS level-set equation and the bounds (t_1, t_2) for the structure were determined using the following expression:

$$-t_1 < r_1 f_1 + r_2 f_2 + \cdots + r_{10} f_{10} < t_2$$

where f_i is *i*-th TPMS level-set equation. In this study, 10 well-known TPMS were utilized (listed in Table 1). To efficiently organize the values of input features, the level-set equations were scaled to have a range between -1 and 1. The proportions ($r_i, i = 1, 2, \ldots, 10$) and bounds t_1 and t_2 were used as input features for our data-driven optimization model, with their values set between 0 and 1.

The volume and mechanical properties of the generated structures were evaluated for using Finite Element Analysis (FEA). Volume was obtained by summing all the element volumes. The effective Young's modulus was calculated via the homogenization method, and obtaining the structure's effective stiffness matrix. These were then converted into relative density and relative Young's modulus, to allow comparison across different structures and materials. The relative properties were calculated through comparison with the properties of the constituent material, using the formula $\bar{C} = C_{structure}/C_{intrinsic}$. These were defined as

objective functions for optimization. The entire process, from HTAM generation to mechanical property evaluation, was automated using MATLAB, Python, and ABAQUS, streamlining data generation and optimization. Initial data was generated as shown in Figure S1. Conventional TPBSs with densities of 20%, 40%, 60%, and 80% were generated. Then, using the concept of HTAM, 20 HTAM structures were created using simple random sampling (SRS) of input features. By leveraging the data from conventional TPBS and SRS-generated HTAM, the optimization model was provided with boundary information from the former and well-distributed data within the design space from the latter.

2.2 Data-Driven Optimization

To efficiently explore the design space and identify optimal structures, generative design strategies, specifically MBO with GPR were employed. Initially, the data collected from initial evaluations was used to fit the GPR surrogate model for each of the two optimization objectives, as shown in Figure S2(a). To refine the model, we introduced Hybrid Monte Carlo, a sampling method derived from Markov Chain Monte Carlo (MCMC) techniques, to tune the GPR hyperparameters. These tunable hyperparameters included likelihood variance, kernel variance, and kernel length scale. The kernel length scale was uniformly configured across all input variables to ensure that the model consistently evaluated interactions between variables, providing a balanced interpretation of the design space. 5000 samplings were conducted and the hyperparameter values corresponding to the peak of Gaussian kernel density estimation were selected as optimal hyperparameters. This method allowed for a more thorough exploration of the parameter space, ultimately improving the accuracy of the surrogate model and the convergence of the optimization process.

Once the GPR model was trained, it was used to differentiate between non-dominated and dominated data points, enabling the establishment of a Pareto front and the analysis of the corresponding hypervolume, as shown in Figure S2(b). This analysis provided insight into the trade-offs between the competing objectives, guiding the optimization process. Based on the Pareto front analyses, acquisition functions were computed to identify regions in the design space where improvements were expected, focusing on areas with the highest acquisition function values. In this study, we adopted a strategy of simultaneously utilizing multiple acquisition functions, specifically PHVI and EHVI. This approach enabled us to strike a balance between exploration, which focuses on reducing the uncertainty of the surrogate model, and exploitation, which targets identifying the optimal design. By employing both acquisition functions concurrently, data efficiency was enhanced, allowing multiple data points to be sampled in each iteration, thus improving overall time efficiency. After each iteration, the two newly suggested structures (one from EHVI and one from PHVI) were generated and evaluated for density and mechanical properties using the automated process outlined in Section 2.1. These results were then incorporated into the existing dataset, allowing the model

to continually learn and refine its predictions. This iterative process continued until an additional 200 data points were generated, as illustrated in Figure 2(c). Through this approach, we were able to thoroughly explore the design space and identify HTAM designs that exhibit superior mechanical performance.

2.3 3D Printing and Compression Testing

To validate the optimization results, optimized HTAM were fabricated using additive manufacturing and tested in compressions. Compression testing was chosen over tensile testing for several reasons. First, the optimization process focused on the linear elastic region, where compression tests are highly effective for evaluating stiffness and load-bearing capacity. Secondly, compression tests are experimentally simpler to conduct, especially for architectured materials.

The selected HTAM structures were open-cell structures to ensure fabrication feasibility. The optimized HTAM, I-WP, and CFCC were chosen, as I-WP exhibited the highest stiffness among TPBS structures, and CFCC demonstrated the highest stiffness among strut-based structures. 3x3x3 unit cell structures were fabricated at relative densities of 0.41 and 0.50.

The structures were fabricated with dimensions of $60\text{mm} \times 60\text{mm} \times 60\text{mm}$ using the Fuse 1+ SLS printer by FORMLABS. The SLS printer was chosen due to its powder-based printing technique, which eliminates the need for support structures and is ideal for fabricating complex geometries with internal voids. After fabrication, the structures were subjected to compression testing using a universal testing machine with a compression jig from SHIMADZU. To ensure consistent and accurate results, the compression rate was set precisely at 0.01 mm/s.

At the micro scale, polymeric microlattices with a $30\ \mu\text{m}$ side length were fabricated on ITO-coated glass cover slips via two-photon-polymerization direct laser writing (TPP-DLW) with the Photonic Professional GT (Nanoscribe GmbH), in dip-in laser lithography (DiLL) mode using a 63x objective lens. IP-Dip photoresist was used with a scanning speed of 10,000 $\mu\text{m/s}$ and laser power of $17.5\ \text{mW}$, and hatching and slicing spacings of $0.1\ \mu\text{m}$. The microlattice samples were developed in Su-8 developer for 30 minutes and isopropyl alcohol for 5 minutes. Then, uniaxial mechanical compression tests were conducted using the iMicro Indentation System (Nanomechanics, Inc.) at a strain rate of $20\ \text{nm/s}$ with a $55\ \mu\text{m}$ diamond flat punch tip. Load-displacement curves were collected and converted to engineering stress-strain curves using the cross-sectional footprint area and initial height of the lattice structures, as measured from high-resolution SEM images using an Apreo S LoVac Scanning Electron Microscope (Thermo Fisher Scientific Inc.). From each engineering stress-strain curve, the Young's modulus was measured from the slope of the linear elastic loading regime, and the

yield strength was measured using the 0.2% offset strain method. Each test for a given relative density and lattice architecture was repeated on three samples, and the resulting values were averaged.

3. Result

3.1 Optimization Result

Tuning the hyperparameters of a Gaussian Process Regression (GPR) model is crucial for improving its predictive accuracy and uncertainty estimation, thereby ensuring robust and reliable performance in the optimization process. In this study, Hybrid Monte Carlo (HMC) was employed to tune the hyperparameters of the GPR model for both optimization objectives—relative density and relative Young's modulus—as shown in Figure 3(a, b). The concentration of sampling points around specific values indicates a robust hyperparameter tuning process, instilling confidence in the accuracy of the fitted GPR model.

The theoretical upper bound in Figure 3(e-g) was determined using the Gibson-Ashby model ($\bar{E} = \bar{\rho}^n$), assuming the Voigt upper bound with $n = 1$. The structures with high relative density on the Pareto front are characterized by central voids within their unit cells. In the Figure 3(e), it is clearly demonstrated that there were no significant improvements in the low relative density region ($\bar{\rho} < 0.4$). The structures that exhibited slight improvements were those with offsets in thickness from the conventional I-WP structure (type 5). This phenomenon arises due to the characteristic nature of the level-set equation, which induces significant changes in the structure as the thickness decreases, thereby increasing the chance to produce a "floating" structure appearance, as shown in Figure S3. Consequently, the design space includes infeasible structures, especially prevalent in low-density regions.

3.2 Effectiveness of Multiple Acquisition Functions

To evaluate the effectiveness of using multiple acquisition functions (MULTI; employing EHVI and PHVI simultaneously), we compared this approach with MBO using either EHVI or PHVI alone. For a fair comparison, each algorithm generated 200 data points starting from the same initial dataset. The distinctive behaviors of these approaches are depicted in Figure 3(e-g). PHVI primarily facilitated exploitation by aggressively pursuing the construction of a Pareto front. However, it often converged to local optima rather than the true global Pareto front, highlighting a limitation in achieving global optimality. On the other hand, EHVI balanced exploration and exploitation, sampling a diverse range of data with varying objective values, which reduced the uncertainty of the surrogate model while also yielding structures near the upper bound.

The use of multiple acquisition functions combined the strengths of both EHVI and PHVI, allowing for a more balanced approach. This resulted in the sampling of data that spanned a broad range of objective values while also identifying designs near Pareto optimality. As a result, the MULTI approach closely approximated the theoretical bound, demonstrating its effectiveness. This trend is further illustrated in Figure 3(c), where the hypervolume indicator—measuring the volume of the objective space dominated by the Pareto front—shows a rapid increase when applying MULTI approach. It converged at the highest value, whereas PHVI converged at a lower value despite a similarly rapid initial increase. EHVI, while slowly increasing the hypervolume indicator, did not fully realize its potential improvement within the limited number of iterations.

Moreover, the MULTI approach demonstrated significant time efficiency. To compare the time performance, we analyzed the average elapsed time per sample until the first 50 data points were generated (Figure 3(d)). The time required for mechanical property evaluation via finite element analysis (FEA) was excluded from this analysis, as the number of elements varied with the sampled structure's shape, potentially introducing bias. The MULTI approach allowed for parallel sampling of two data points per iteration, reducing the required time by 32%. In contrast, PHVI and EHVI, which sampled one data point per iteration, required more processing time. This time difference arose from fewer GPR fittings required in the MULTI approach. Although the computational complexity of EHVI was higher, PHVI exhibited longer processing times and greater variance due to its strong focus on exploitation, which increased the number of non-dominated data points over iterations and extended the processing time.

To more precisely compare the performance of each algorithm, we quantified their effectiveness using Sampling Error (SE) and Distribution Metric (DM), with detailed descriptions provided in the supplementary material. SE measures how close the sampled data are to the true Pareto front, while DM quantifies the uniformity of the sampling distribution within the objective space. As shown in Figure S4, EHVI achieved the lowest mean SE, reflecting its tendency to explore boundaries and reduce GPR uncertainty. This often resulted in designs with relative densities of 0 or 1, which are part of the true Pareto front, thus yielding lower SE. However, EHVI performed poorly in terms of DM, indicating uneven sampling distribution. In contrast, the MULTI approach showed lower SE, indicating effective exploration, and lower DM, signifying well-distributed sampling. This combination proved to be the most efficient optimization strategy, balancing both exploration and exploitation, and resulted in a Pareto front that was both close to the theoretical bound and well-distributed across the design space.

3.3 Validation of Mechanical Properties

FEA was used to further validate the properties of optimal HTAM, and compare the properties to I-WP and CFCC, as depicted in Figure 4(a-d). For structures with 41% density,

FEA confirmed the relative Young's modulus of these structures as 0.255, 0.240, and 0.150, respectively. For the 50% density structures, the relative Young's modulus was found to be 0.336, 0.271, and 0.209, respectively. These results confirm HTAM's superior mechanical properties within the linear elastic range. These results indicate that HTAM maintain higher stiffness-to-density ratios compared to other configurations, which is critical for applications requiring lightweight yet strong materials.

The stress distribution within the optimized HTAM was compared to I-WP and CFCC, as shown in Figure 4(e). The analysis of the stress distribution is essential to understanding the durability and failure modes of the structures. The CFCC structure exhibited high stress concentrations at many joints. The HTAM and I-WP structures exhibited high stress concentrations at fewer locations. This indicates a more uniform distribution of stress across the structure, reducing the likelihood of localized failure and improving overall mechanical performance as shown in Figure 4(f).

3.4 Experimental Validation of Optimization Result

To validate the optimization results, structures with relative densities of 0.41 and 0.5 were modeled and printed using an SLS printer, as shown in Figure 5(a, b). The results of the SLS printing demonstrated that the fabricated structures closely resembled the modeled designs. This outcome validated the precision of the SLS technique, which is known for its ability to produce complex geometries with high fidelity. The strain-stress curve for these structures was obtained through compression testing, as depicted in Figure 5(c, d). The results indicated that the effective stiffness is highest for the HTAM structure, followed by I-WP, and then CFCC. This trend in effective stiffness agrees with computational simulation.

This trend was also observed in structures fabricated using 2PP. Figure 6(a, b) shows scanning electron microscope images of HTAM, I-WP, and CFCC microlattices with $\rho = 0.41$ and 0.5. For both relative densities, engineering stress-strain curves (Figure 6(c, d)) reveal that the HTAM microlattices have the stiffest linear elastic loading response and the greatest initial strain hardening, followed by the I-WP structure and finally the CFCC structure. At strains around $\varepsilon = 0.4$, the HTAM lattice exhibits softening up to eventual densification (for $\rho = 0.41$) or failure (for $\rho = 0.50$). Comparatively, the I-WP and CFCC lattices exhibit minimal softening before densification. Figure 6(e, f) show the Young's modulus and yield strength values measured from engineering stress-strain curves. As expected, the HTAM lattices exhibit the highest elastic moduli and yield strengths at both relative densities, followed by the I-WP and finally the CFCC lattices.

These results indicate that the optimized HTAM has the highest stiffness regardless of the scale of the 3D printed structure. Additionally, beyond elastic region, HTAM exhibited the highest effective yield strength, followed by I-WP, and then CFCC. The higher effective

stiffness of HTAM indicates a greater resistance to applied forces, meaning the structure can distribute stress more evenly under load. This uniform stress distribution is a key factor contributing to the increased effective yield strength, as it delays the onset of plastic deformation, given that the material is the same across all structures. After the yield point, distinct behaviors were observed in the SLS and 2PP structures. In the SLS structures, catastrophic failure occurred shortly after the yield point. In contrast, the 2PP structures exhibited densification after yielding, a phenomenon where the structure compacts rather than fractures. This difference is explained by the materials used: the material in the 2PP process is relatively more ductile compared to the brittle material used in SLS printing, leading to the observed differences in post-yield behavior.

4. Conclusion

The optimized HTAM structure marks a significant advancement in the development of architectured materials. We demonstrate a novel approach to customizing material properties. By combining multiple TPMS level-set equations, HTAM opens up a vast design space previously inaccessible with singular TPMS structures. The use of MBO with multiple acquisition functions proved to be an effective method for exploring and optimizing HTAM configurations. This approach facilitated simultaneous optimization of various objectives, constructing Pareto fronts characterized by trade-offs between stiffness and weight, ultimately leading to the discovery of superior HTAM designs with higher specific Young's modulus compared to conventional TPMS and strut-based structures.

The feasibility of fabricating these complex HTAM was successfully demonstrated through 3D printing techniques at both macro and micro scales, utilizing SLS and 2PP. The printed structures closely matched the initial computational models, confirming the accuracy and reliability of the fabrication processes. Compression testing validated the exceptional mechanical performance of HTAM, with higher stiffness and yield strength observed compared to traditional TPMS and strut-based counterparts. A similar level of performance was observed in macro and microscale structures, which underscores the robustness of the design and optimization approach.

This study demonstrates that the integration of advanced generative design strategies with precise manufacturing techniques can lead to significant improvements in material performance. These findings highlight the potential of HTAM to meet the growing demands for strong, lightweight materials, particularly in industries where material efficiency is critical, such as aerospace, automotive, and biomedical engineering. Additionally, the post-yield behavior differences observed between macro and micro scales emphasize the importance of material selection in determining the mechanical performance of architectured materials. Further exploration of these behaviors could open new avenues for tailoring material properties to specific applications.

Acknowledgements and funding section?

5. Reference

1. Begley, M.R., et al., *Micromechanical models to guide the development of synthetic 'brick and mortar' composites.* Journal of the Mechanics and Physics of Solids, 2012. **60**(8): p. 1545-1560.
2. Kim, Y., et al., *An extended analytic model for the elastic properties of platelet-staggered composites and its application to 3D printed structures.* Composite Structures, 2018. **189**: p. 27-36.
3. Park, K., et al., *Multi-objective Bayesian optimization for the design of nacre-inspired composites: optimizing and understanding biomimetics through AI.* Materials Horizons, 2023. **10**(10): p. 4329-4343.
4. Zhao, H. and L. Guo, *Nacre-inspired structural composites: performance-enhancement strategy and perspective.* Advanced Materials, 2017. **29**(45): p. 1702903.
5. Yang, Y., et al., *Recent progress in biomimetic additive manufacturing technology: from materials to functional structures.* Advanced Materials, 2018. **30**(36): p. 1706539.
6. Yeo, S.J., M.J. Oh, and P.J. Yoo, *Structurally controlled cellular architectures for high-performance ultra-lightweight materials.* Advanced Materials, 2019. **31**(34): p. 1803670.
7. Hu, Q., et al., *Constructing coral-like hierarchical porous carbon architectures with tailored pore size distribution as sulfur hosts for durable Li-S batteries.* Electrochimica acta, 2021. **377**: p. 138063.
8. Zhao, X., et al., *Fabrication, characteristics and applications of carbon materials with different morphologies and porous structures produced from wood liquefaction: A review.* Chemical Engineering Journal, 2019. **364**: p. 226-243.
9. Wang, X., et al., *Topological design and additive manufacturing of porous metals for bone scaffolds and orthopaedic implants: A review.* Biomaterials, 2016. **83**: p. 127-141.
10. Hanks, B., et al., *Mechanical properties of additively manufactured metal lattice structures: Data review and design interface.* Additive Manufacturing, 2020. **35**: p. 101301.
11. Thompson, M.K., et al., *Design for Additive Manufacturing: Trends, opportunities, considerations, and constraints.* CIRP annals, 2016. **65**(2): p. 737-760.
12. Kladovasilakis, N., et al., *Architected materials for additive manufacturing: A comprehensive review.* Materials, 2022. **15**(17): p. 5919.
13. Traxel, K.D. and A. Bandyopadhyay, *Naturally architected microstructures in structural materials via additive manufacturing.* Additive manufacturing, 2020. **34**: p. 101243.
14. Greer, J.R. and V.S. Deshpande, *Three-dimensional architected materials and structures: Design, fabrication, and mechanical behavior.* MRS Bulletin, 2019. **44**(10): p. 750-757.
15. Barthelat, F., *Architectured materials in engineering and biology: fabrication, structure, mechanics and performance.* International Materials Reviews, 2015. **60**(8): p. 413-430.
16. Mao, Y., Q. He, and X. Zhao, *Designing complex architectured materials with generative adversarial networks.* Science advances, 2020. **6**(17): p. eaaz4169.
17. Zheng, L., S. Kumar, and D.M. Kochmann, *Data-driven topology optimization of spinodoid metamaterials with seamlessly tunable anisotropy.* Computer Methods in Applied Mechanics and Engineering, 2021. **383**: p. 113894.
18. Yu, X., et al., *Mechanical metamaterials associated with stiffness, rigidity and compressibility: A brief review.* Progress in Materials Science, 2018. **94**: p. 114-173.
19. Frenzel, T., M. Kadic, and M. Wegener, *Three-dimensional mechanical metamaterials*

with a twist. Science, 2017. **358**(6366): p. 1072-1074.
20. Kadic, M., et al., *On the practicability of pentamode mechanical metamaterials.* Applied Physics Letters, 2012. **100**(19).
21. Bose, S., et al., *Additive manufacturing of biomaterials.* Progress in materials science, 2018. **93**: p. 45-111.
22. Markl, D., et al., *Characterisation of pore structures of pharmaceutical tablets: A review.* International journal of pharmaceutics, 2018. **538**(1-2): p. 188-214.
23. Camacho, D.D., et al., *Applications of additive manufacturing in the construction industry–A forward-looking review.* Automation in construction, 2018. **89**: p. 110-119.
24. Lee, W., et al., *Controlled unusual stiffness of mechanical metamaterials.* Scientific reports, 2016. **6**(1): p. 20312.
25. Rezapourian, M., N. Kamboj, and I. Hussainova. *Numerical study on the effect of geometry on mechanical behavior of triply periodic minimal surfaces*. in *IOP Conference Series: Materials Science and Engineering*. 2021. IOP Publishing.
26. Ramírez, E., et al., *Design parameters effects on relative density of triply periodic minimal surfaces for additive manufacturing.* Procedia CIRP, 2021. **100**: p. 13-18.
27. Blanquer, S.B., et al., *Surface curvature in triply-periodic minimal surface architectures as a distinct design parameter in preparing advanced tissue engineering scaffolds.* Biofabrication, 2017. **9**(2): p. 025001.
28. Montemayor, L. and J. Greer, *Mechanical response of hollow metallic nanolattices: combining structural and material size effects.* Journal of Applied Mechanics, 2015. **82**(7): p. 071012.
29. Crook, C., et al., *Plate-nanolattices at the theoretical limit of stiffness and strength.* Nature communications, 2020. **11**(1): p. 1579.
30. Feng, J., et al., *Triply periodic minimal surface (TPMS) porous structures: from multi-scale design, precise additive manufacturing to multidisciplinary applications.* International Journal of Extreme Manufacturing, 2022. **4**(2): p. 022001.
31. Rajagopalan, S. and R.A. Robb, *Schwarz meets Schwann: design and fabrication of biomorphic and durataxic tissue engineering scaffolds.* Medical image analysis, 2006. **10**(5): p. 693-712.
32. Portela, C.M., J.R. Greer, and D.M. Kochmann, *Impact of node geometry on the effective stiffness of non-slender three-dimensional truss lattice architectures.* Extreme Mechanics Letters, 2018. **22**: p. 138-148.
33. Meza, L.R., S. Das, and J.R. Greer, *Strong, lightweight, and recoverable three-dimensional ceramic nanolattices.* Science, 2014. **345**(6202): p. 1322-1326.

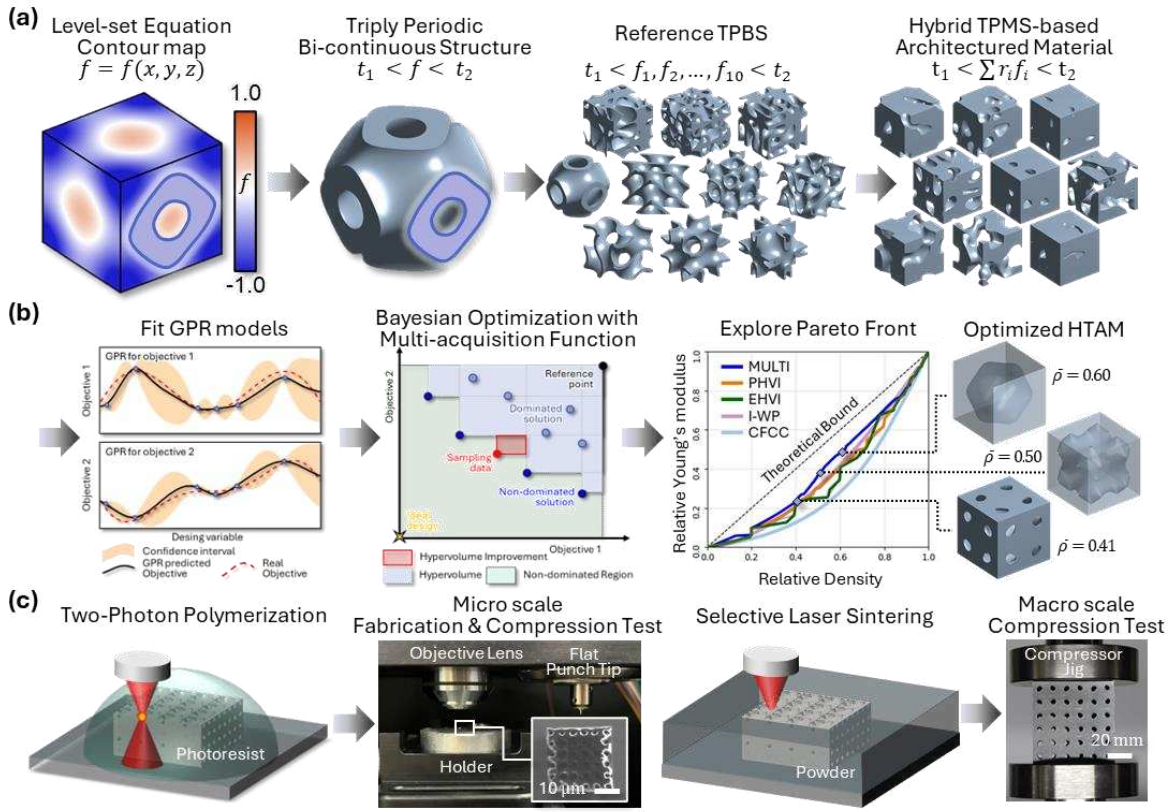

Figure 1. Hybrid TPMS-based Architectured Material (HTAM), multi-objective Bayesian optimization, and validation through additive manufacturing. (a) Illustration of process for defining HTAM: contour map of the level-set equation, structures constructed based on the volume corresponding to the level-set values, 10 well-known TPBS (I-WP, Neovius, Schwarz P, Schwarz D, Fisher-Koch Y, F-RD, Fisher-Koch C(S), Gyroid, Fisher-Koch S, Fisher-Koch C(Y)) used as reference structures, and randomly generated HTAMs. (b) Schematic of the multi-objective Bayesian optimization process. (c) Additive manufacturing technologies for micro-scale and macro-scale fabrication, and compression testing.

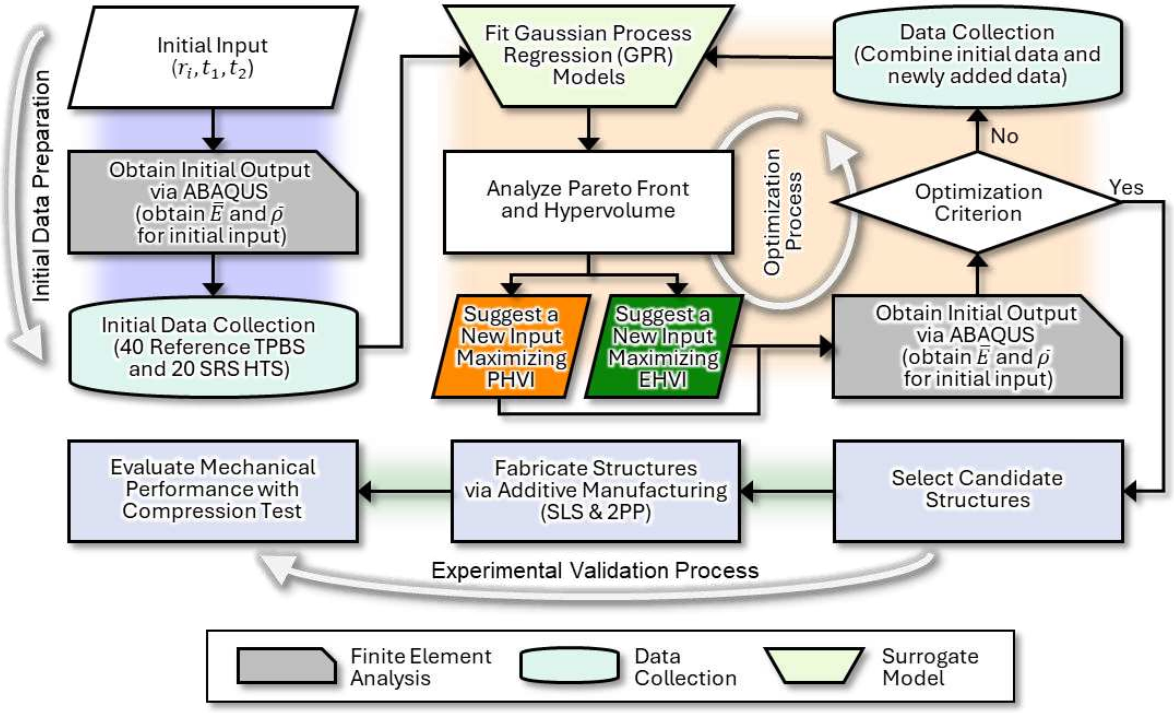

Figure 2. Multi-objective Bayesian Optimization (MBO) with Gaussian Process Regression (GPR) Schematic Diagrams. Workflow chart of the multi-objective Bayesian optimization framework with multiple acquisition functions, detailing the steps from the preparation of initial data, through the optimization process, to the validation process.

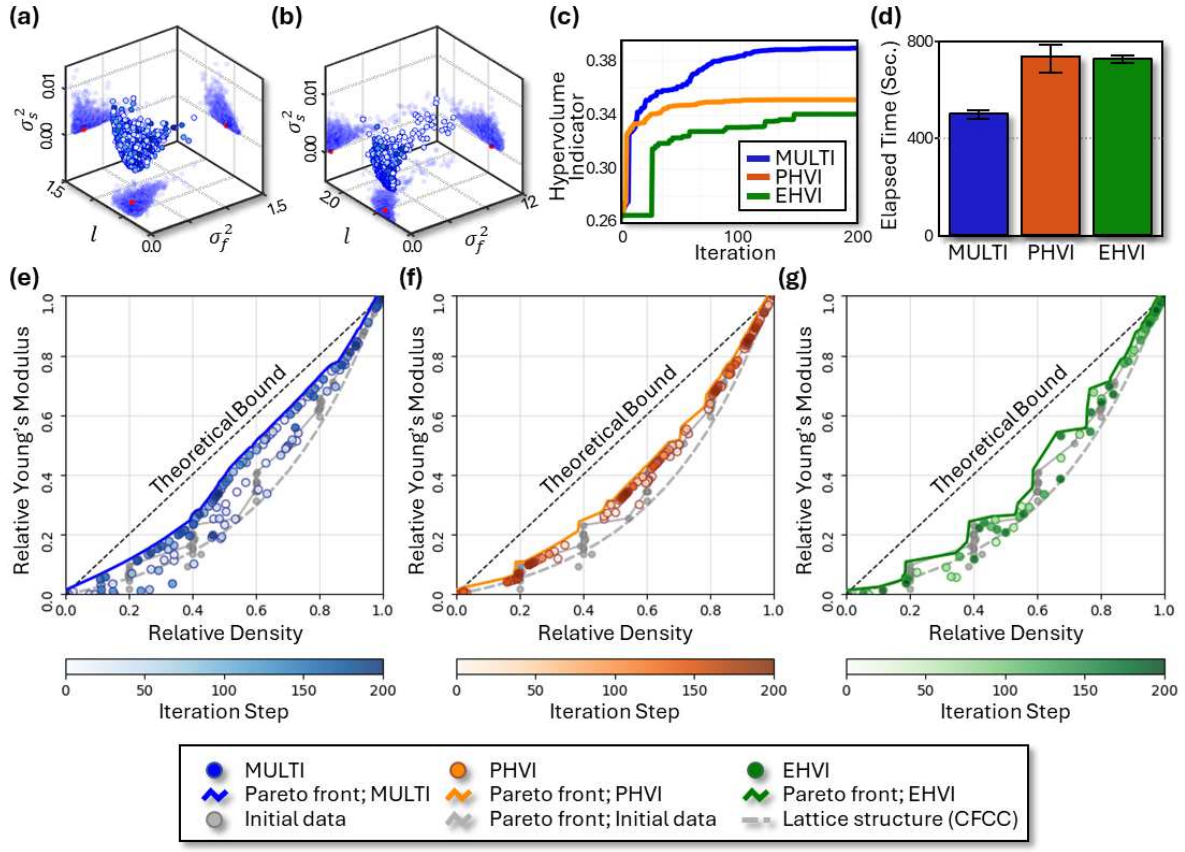

Figure 3. Hyperparameter Tuning and Comparison of Optimization Performance (a, b) Results of Hybrid Monte Carlo, with the red point indicating the tuned hyperparameter: l(kernel length scale), σ_f(kernel variance), and σ_s(likelihood variance). (c) Hypervolume indicator for Multi, PHVI, and EHVI as a function of iteration. (d) Comparison of the elapsed time for sampling until 50 points are obtained using Multi, PHVI, and EHVI. (e-g) Scatter plot and Pareto front for Multi, PHVI, and EHVI data for relative density and relative Young's modulus, compared with the initial data and lattice structure (CFCC).

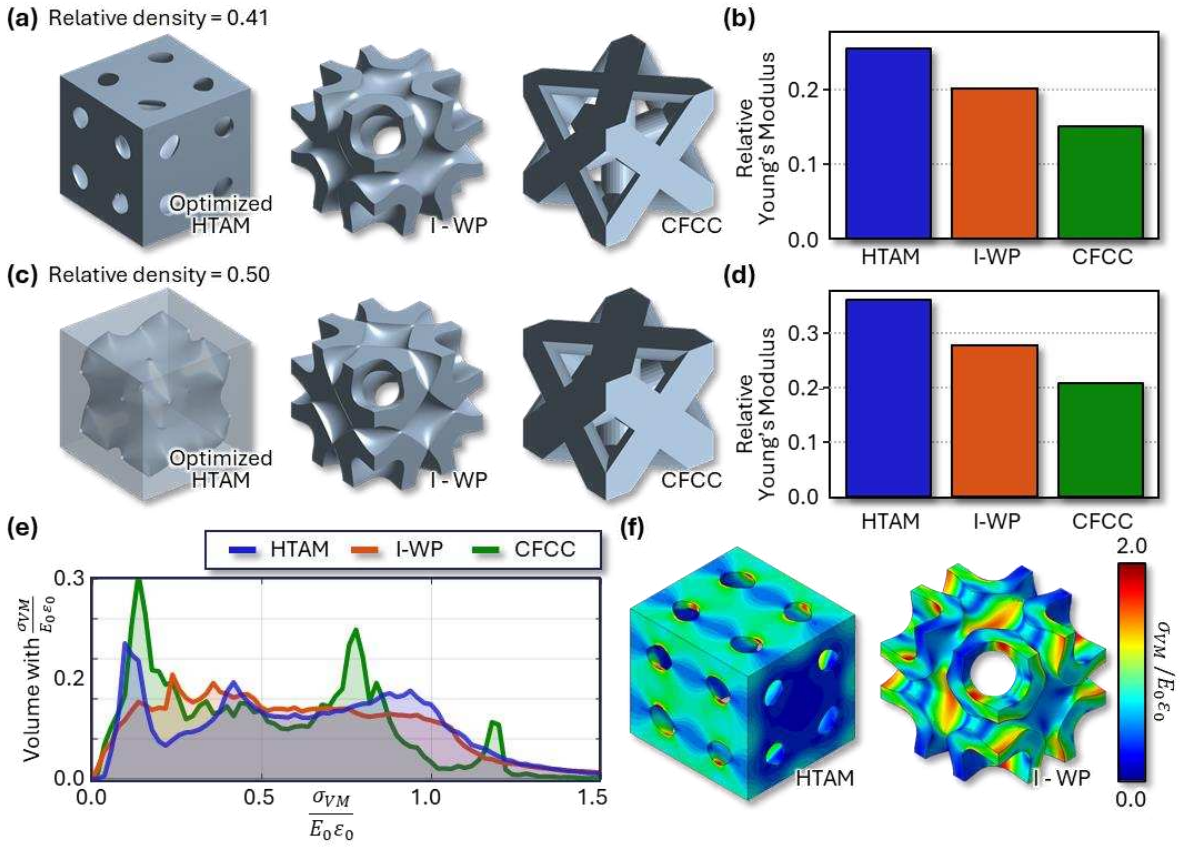

Figure 4. Comparison between HTAM, I-WP (a TPBS structure), and Strut-Based Structure (CFCC). (a, c) Structures with relative densities of 0.41 and 0.50. (b, d) Relative Young's modulus with relative densities of 0.41 and 0.50. (e) Volume distribution plot of normalized Von Mises stress in structures with a relative density of 0.41. (f) FEA compression of HTAM and I-WP with a relative density of 0.41.

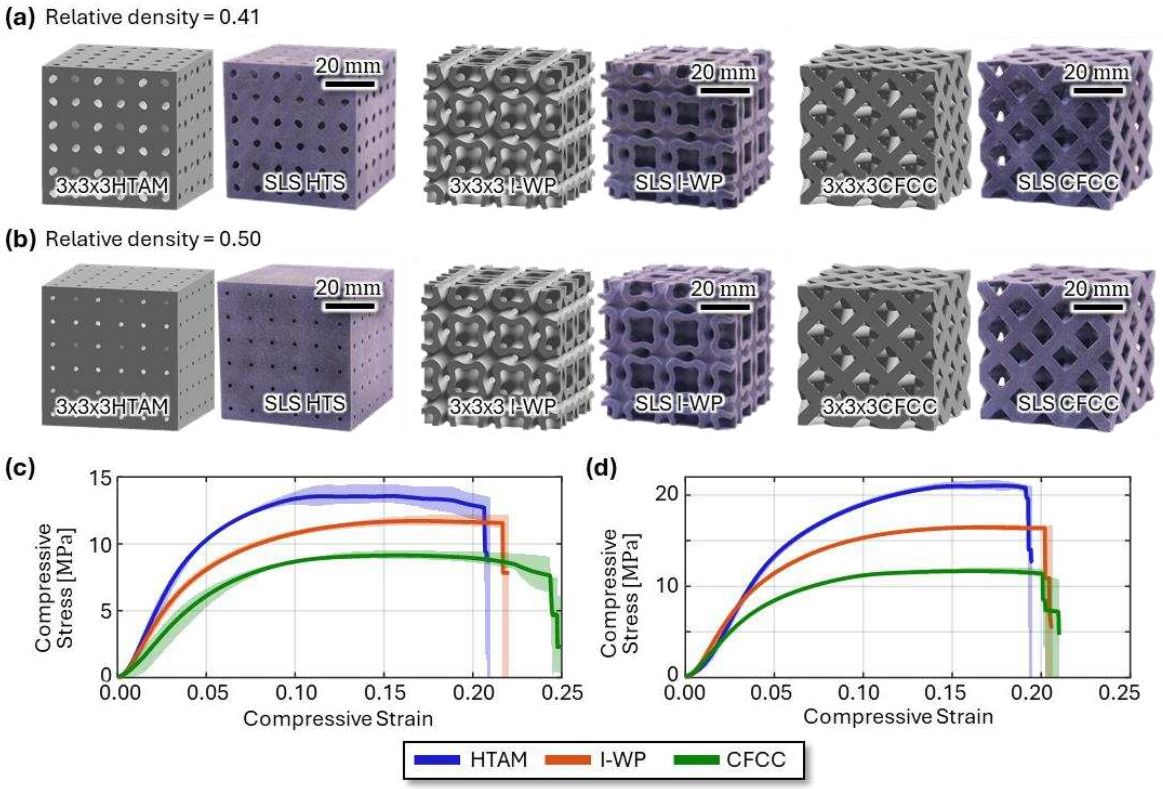

Figure 5. SLS Printing and Compression Testing. (a, b) Structures modeled with unit cells arranged in a 3x3x3 configuration and relative densities of 0.41 and 0.50, along with their SLS printed products. (c, d) Compressive strain-stress curves for structures with relative densities of 0.41 and 0.50, respectively.

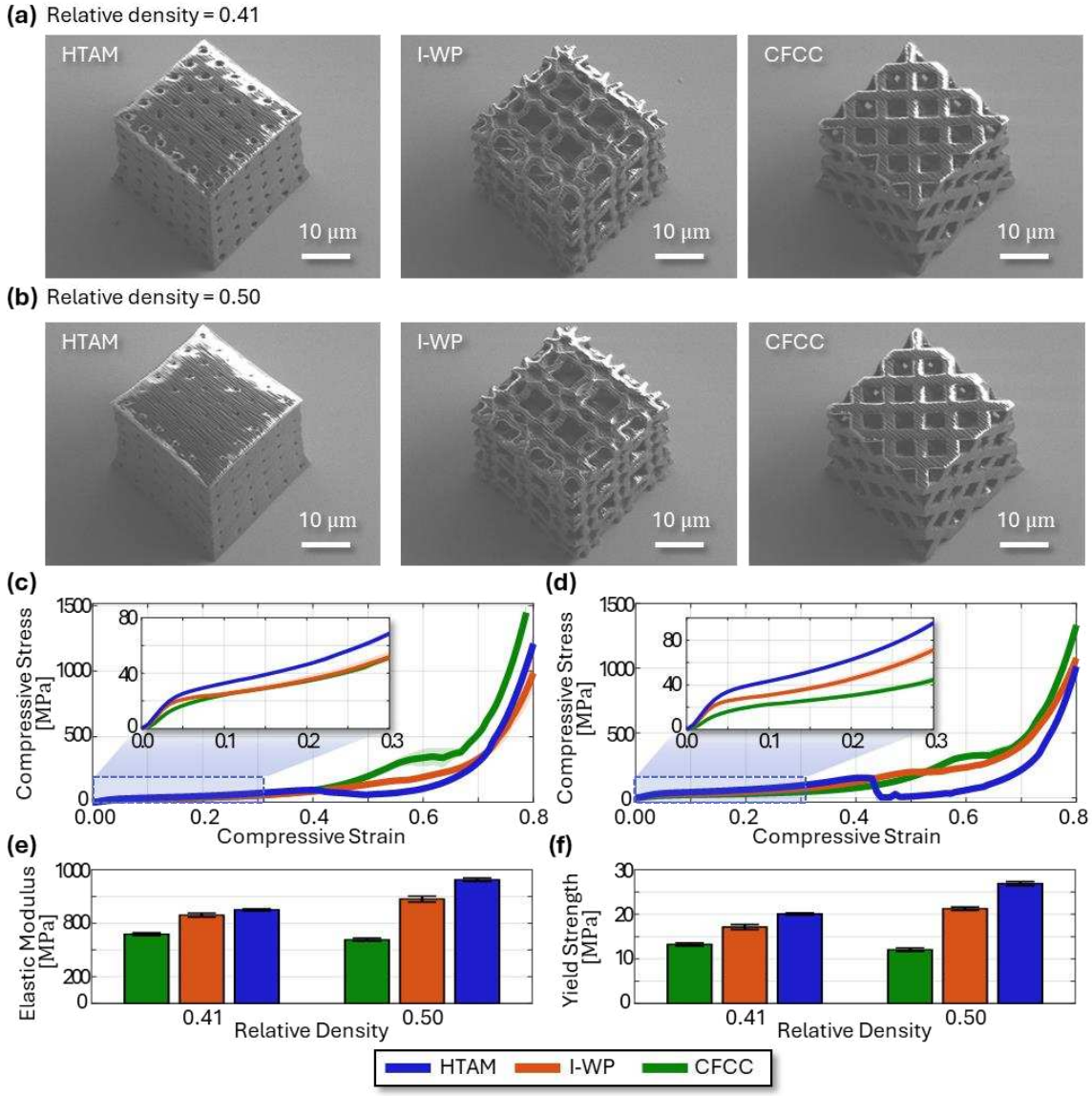

Figure 6. 2PP Printing and Compression Testing. (a-b) Scanning electron microscope images of polymeric microlattices, with HTAM, I-WP, and CFCC architectures, fabricated at a relative density of 0.41 and 0.50, respectively. (c, d) Compressive stress-strain curves for polymeric microlattices at relative densities of 0.41 and 0.50, respectively. Insets show the same engineering stress-strain curves up to strains of $\varepsilon = 0.3$. (e, f) Measured Young's modulus values and yield strengths for the three microlattice architectures at a relative density of 0.41 and 0.50, respectively.

Table 1. List of TPMS level-set equations used in defining HTAM.

TPMS	**Level-set equation,** $f_i = 0$
Schwarz P	$f_1 = \cos(x) + \cos(y) + \cos(z) = 0$
Schwarz D	$f_2 = \sin(x)\sin(y)\sin(z) + \sin(x)\cos(y)\cos(z) + \cos(x)\sin(y)\cos(z) + \cos(x)\cos(y)\sin(z) = 0$
Gyroid	$f_3 = \cos(x)\sin(y) + \cos(y)\sin(z) + \cos(z)\sin(x) = 0$
Neovius	$f_4 = 3(\cos(x) + \cos(y) + \cos(z)) + 4\cos(x)\cos(y)\cos(z) = 0$
I-WP	$f_5 = 2(\cos(x)\cos(y) + \cos(y)\cos(z) + \cos(z)\cos(x)) - (\cos(2x) + \cos(2y) + \cos(2z)) = 0$
F-RD	$f_6 = 4\cos(x)\cos(y)\cos(z) - (\cos(2x)\cos(2y) + \cos(2y)\cos(2z) + \cos(2x)\cos(2z)) = 0$
Fisher-Koch S	$f_7 = \cos(2x)\sin(y)\cos(z) + \sin(x)\cos(2y)\sin(z) + \sin(x)\sin(y)\cos(2z) = 0$
Fisher-Koch C(S)	$f_8 = \cos(2x) + \cos(2y) + \cos(2z) + 2(\sin(3x)\sin(2y)\cos(z) + \cos(x)\sin(3y)\sin(2z) + \sin(2x)\cos(y)\sin(3z) + 2(\sin(2x)\cos(3y)\sin(z) + \sin(x)\sin(2y)\cos(3z) + \cos(3x)\sin(y)\sin(2z)) = 0$
Fisher-Koch Y	$f_9 = \cos(x)\cos(y)\cos(z) + \sin(x)\sin(y)\sin(z) + \sin(2x)\sin(y) + \sin(2y)\sin(z) + \sin(x)\sin(2z) + \sin(2x)\cos(z) + \sin(2y)\cos(x) + \sin(2z)\cos(y) = 0$
Fisher-Koch C(Y)	$f_{10} = -\sin(x)\sin(y)\sin(z) + \sin(2x)\sin(y) + \sin(2y)\sin(z) + \sin(2z)\sin(x) - \cos(x)\cos(y)\cos(z) + \sin(2x)\cos(z) + \cos(x)\sin(2y) + \cos(y)\sin(2z) = 0$

Supplementary Information

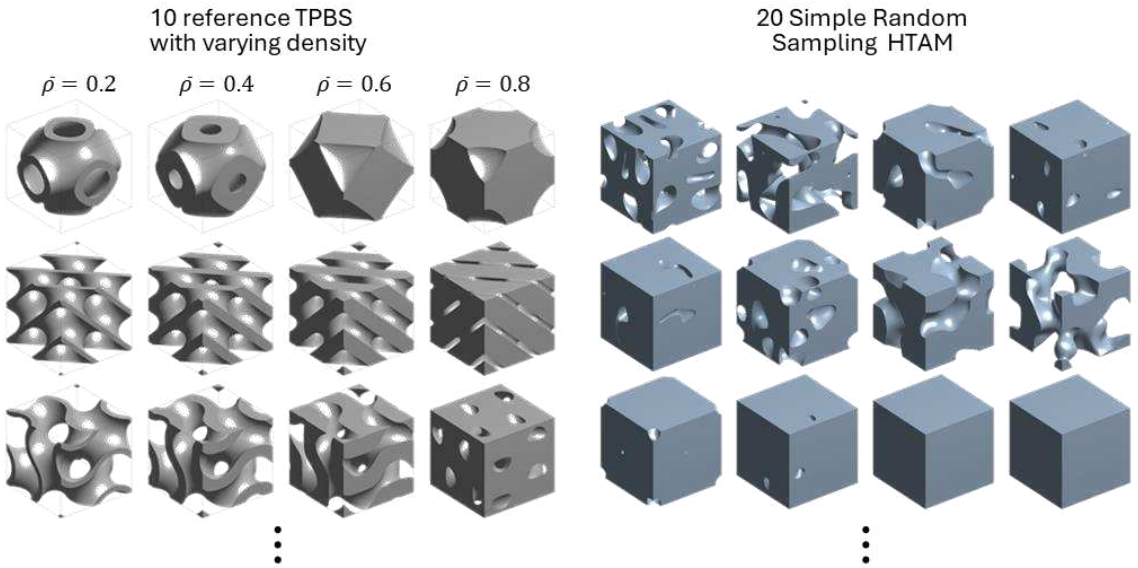

Figure S1. Initial structures for Multi Bayesian Optimization (MBO) with Gaussian Process Regression (GPR). The structures on the left are based on reference TPBS, while the structures on the right are constructed based on the definition of HTAM.

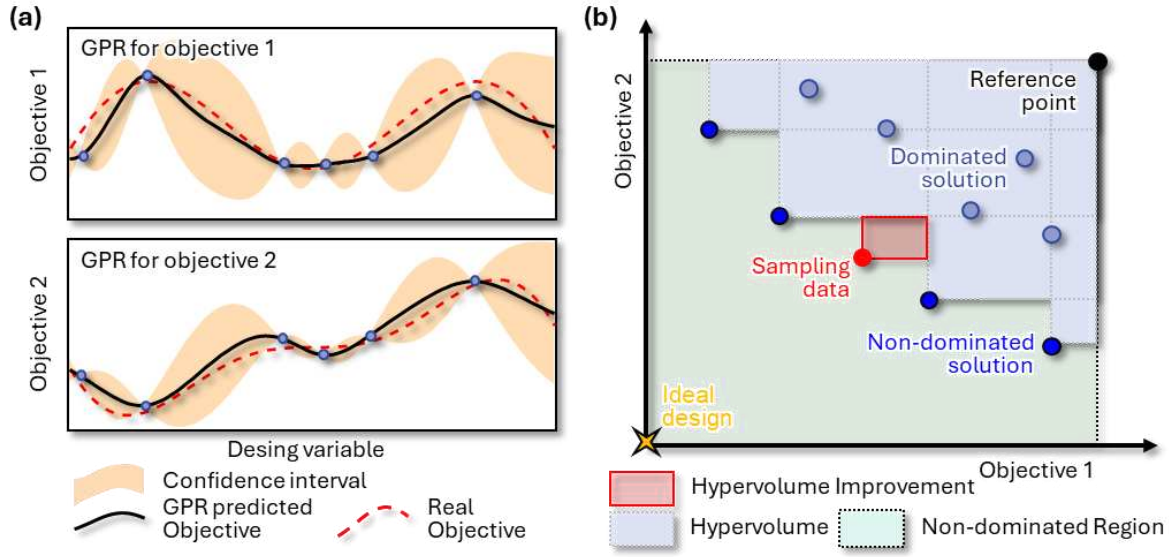

Figure S2. (a) A graphical representation of the Gaussian Process Regression model for multiple objectives. (b) A graphical representation of multi-objective Bayesian optimization in the 2D objective space.

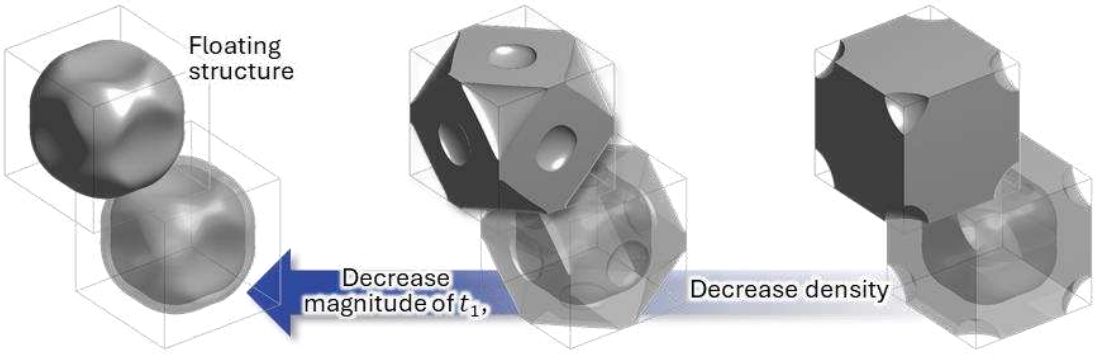

Figure S3. Illustration showing the emergence of floating structures as density decreases. As the density reduces, the level-set equations generate structures with disconnected or isolated elements, leading to the formation of "floating" structures that are not connected to the main framework.

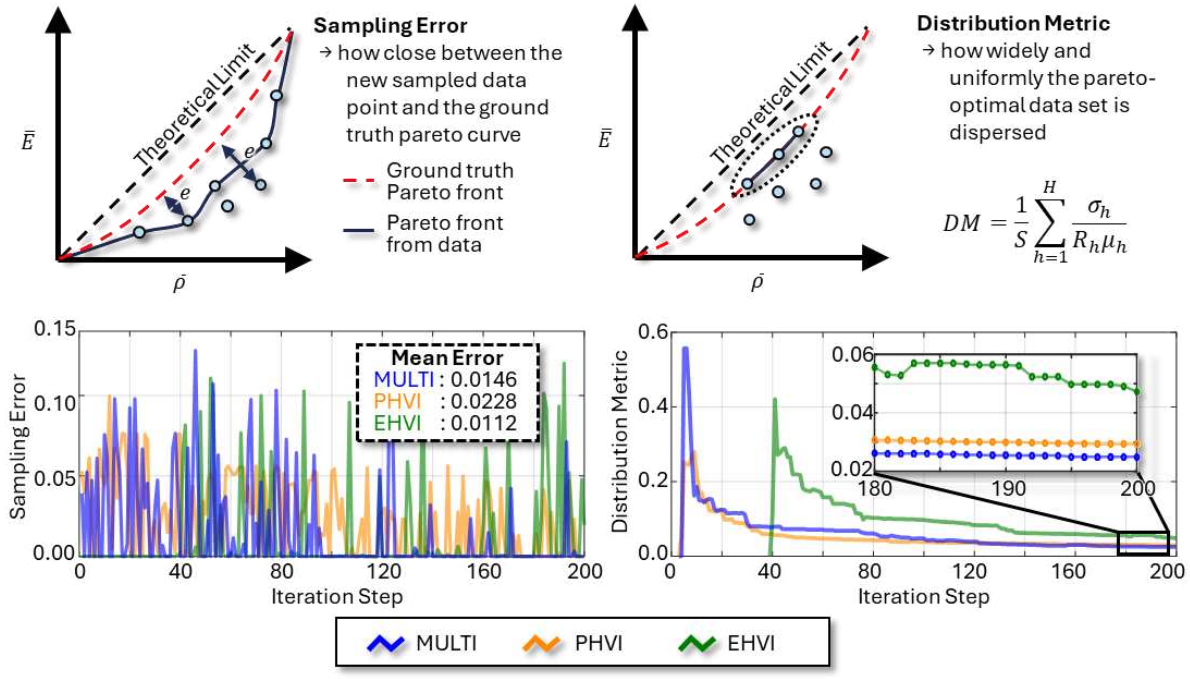

Figure S4. Illustration of Sampling Error (SE) and Distribution Metric (DM) concepts. Evaluation results of SE and DM for Multi, EHVI, and PHVI are also included. This figure demonstrates how each acquisition function performs in terms of proximity to the ground truth Pareto front and the uniformity of sampling distribution in the objective space.